Available online at www.sciencedirect.com
ScienceDirect
Journal of Marine Systems 66 (2007) 61–70
JOURNAL OF MARINE SYSTEMS
www.elsevier.com/locate/jmarsys

Characteristics of bubble plumes, bubble-plume bubbles and waves from wind-steepened wave breaking

Ira Leifer [a,*], Guillemette Caulliez [b,1], Gerrit De Leeuw [c,2]

[a] *Marine Science Institute, University of California, Santa Barbara, Santa Barbara, CA, 93106-1080, USA*
[b] *Institut de Recherche sur les Phenomenes Hors Equilibre, 163 avenue de Luminy- case 903, 13288 Marseille Cedex 9, France*
[c] *TNO, P.O. Box 96864, 2509 JG The Hague, The Netherlands*

Received 4 October 2005; accepted 10 January 2006
Available online 26 January 2007

Abstract

Observations of breaking waves, associated bubble plumes and bubble-plume size distributions were used to explore the coupled evolution of wave-breaking, wave properties and bubble-plume characteristics. Experiments were made in a large, freshwater, wind-wave channel with mechanical wind-steepened waves and a wind speed of 13 m s^{-1}. Bubble plumes exhibited a wide range of bubble distributions, physical extent and dynamics. A classification scheme was developed based on plume extent and "optical density" which is the ability of a plume to optically obscure the image of the background until maximum penetration of the plume. Plumes were classified as either dense (obscure) or diffuse (no-obscure). For each class, the plume bubble population size distribution, $\Phi(r,t)$, where r is the bubble radius and t the time, was determined. Dense plumes have a large radius peak in Φ and thus are enhanced in large bubbles. Diffuse plumes are well-described by a weakly size decreasing $\Phi(r,t)$ for $r<1000$ µm and a more strongly size decreasing $\Phi(r,t)$ for $r>1000$ µm.

The bubble-plume formation rate, P, for each class, wave-breaking rate and wave characteristics were measured with respect to fetch. Wave-breaking rate and intensity are strongly fetch-dependent. In general, the trends in P and wave breaking are similar, reaching a maximum at the fetch of maximum wave breaking. The ratio of P for dense to diffuse plumes is even more sensitive to the occurrence of the most intense wave breaking, where dense plume formation is the greatest.

Using P and the bubble size population distributions for each plume class, the global bubble-plume, injection size distribution, $\Psi_i(r)$, was calculated. The volume injection rate for the study area was 640 cm^3 s^{-1} divided approximately equally between bubbles smaller and larger than $r\sim1700$ µm.

1. Introduction

Bubbles generated by breaking waves either play a dominant or significant role in numerous diverse geophysical processes including air–sea gas transfer (Woolf, 1997), turbulence generation (Kitaigorodskii, 1984), aerosol formation (De Leeuw, 1990), sea-surface microlayer enrichment (Liss et al., 1997) and the transformation of dissolved organic material to particulate organic material (Monahan and Dam, 2001; O'Dowd

* Corresponding author. Tel.: +1 805 893 4941; fax: +1 805 893 4731.
E-mail addresses: ira.leifer@bubbleology.com (I. Leifer), caulliez@irphe.univ-mrs.fr (G. Caulliez), deleeuw@fel.tno.nl (G. De Leeuw).
[1] Tel.: +33 491 82 80 06; fax: +33 491 41 96 20.
[2] Tel.: +31 70 374 0462; fax: +31 70 374 0654.

0924-7963/$ - see front matter
doi:10.1016/j.jmarsys.2006.01.011

et al., 2004). Breaking wind-wave bubbles span a wide size range, from smaller than 20 μm (Medwin and Breitz, 1989) to order 1.0 cm diameter (Leifer et al., 2006), covering a wide range of Reynolds numbers (0.05 to 4×10^3) and consequently a wide range of efficiencies for various bubble processes (Clift et al., 1978).

The vast majority of bubble measurements are time and spatially averaged. As a result, these measurements are of the quasi steady-state background population, which primarily consists of small bubbles. However, the source of the background population is the bubble-plume remnants, which are distinctly different. Bubble plumes contain many large bubbles, have much higher bubble concentrations and are transient (Leifer and De Leeuw, 2006). While for some processes the background population is the most important (e.g., acoustic scattering), plume bubbles may dominate for others (e.g., soluble gas transfer). Therefore, assessing the significance of a bubble-mediated process requires measurement of the appropriate size distribution—plume or background. The background size distribution varies with many factors including wind speed, water temperature, salinity, fetch (De Leeuw and Cohen, 2002) and wave-breaking mechanism (e.g., wave breaking due to wind stress, interaction with the bottom in the surf zone or wave modulation). Because the bubble plumes are the source of the background population, it is likely that the bubble-plume size distribution also varies with factors that affect wind stress and hence wave development. This paper presents observations of bubble-plume bubbles, bubble plumes and wave characteristics for wind-steepened mechanical breaking waves in a large freshwater wind-wave tank, for constant wind speed. Thus, variations in bubble-plume and bubble formation were due to change in wave development.

2. Methods

The study was part of the LUMINY experiment, which investigated the relative importance of waves, turbulence, and bubble plumes to air–water gas transfer for a variety of wind and wave conditions. The LUMINY study was in the Large Air–Sea Interaction Simulation Tunnel of the Institut de Recherche sur les Phénomènes Hors Equilibre (IRPHE-IOA), in Marseille-Luminy, France and is described in detail in De Leeuw et al. (1996, 2002). In brief, measurements of air–water gas transfer were made in a 2.5-m high by 2.6-m wide by 40-m long wind-wave channel filled to 0.9 m with UV-sterilized, filtered, freshwater; however, water quality rapidly decreased during the experiments. For the bubble-plume studies, the wind speed was 13 m s^{-1} with mechanically generated waves of 1.2 Hz and 1.3-m wavelength. Instrumentation to measure bubble size distributions, wave characteristics and airflow properties was mounted on a carriage that could move along the tank (Caulliez, 2002).

Bubbles observations were made with two complementary optical bubble measurement systems (BMS). A non-invasive BMS measured plume bubbles and plume characteristics over the size range 150–5000 μm. In the plumes, bubble density was very high, and bubbles were analyzed by hand and tracked between frames to identify hidden bubbles and size out of focus bubbles when in-focus. A constrained measurement-volume BMS measured the background bubble population over the size range 10 to 500 μm. Both BMSs, analysis methodology and calibrations are described in detail in Leifer et al. (2003) and Leifer and De Leeuw (2006).

In brief, the non-invasive BMS used multiple-underwater video cameras to simultaneously observe bubble distributions at multiple resolutions for one or several locations. Multiple lights behind two screens provided very even back-illumination. Components were mounted on a frame that maintained the main camera axes perpendicular to the wind direction. An overview camera observed the measurement volume with a wide field of view from a different angle than the main cameras. The overview camera imaged entire plumes and also ensured that any bubbles produced by the housings were not advected into the measurement volume.

Videos were digitized into short clips of in-focus plumes. Images were thresholded and largely analyzed by hand on a Macintosh computer with the aid of routines written for the public domain software NIH Image (NIH Software, 2001). Due to the high void fraction–which caused touching and overlapping bubbles–and irregular shape of large bubbles, manual bubble analysis often is required within the bubble plume (Haines and Johnson, 1995). Where possible, bubbles were tracked manually between frames. This allowed identification of partially or completely obscured bubbles. The outline of an obscured bubble generally could be identified through the forward bubble, aided by routines that predicted each bubble location in subsequent frames. Small bubbles, which were blurred due to motion, were sized at or near their maximum injection depth when they were nearly motionless. Bubbles at the edge of the in-focus region often were blurry and were sized when in-focus or were not counted.

Using a least-squares linear-regression analysis, the best fit ellipse was calculated for each bubble outline, providing the major and minor axes and angle. The equivalent spherical radius, r, was calculated from the two axes. From the time sequences of r, time-resolved bubble size distributions were calculated from histograms using routines written in Matlab (Mathworks, MA). Size histograms were calculated for each time interval and radius bins were logarithmically spaced, spanning 100-μm to 5000-μm radius. Size distributions were normalized to units of μm^{-1}.

Bubble plumes were segregated based on plume horizontal extent, w, penetration depth, z_P, and ability to optically obscure (termed dense) or not obscure (termed diffuse) the image background (i.e., the image background was not visible behind the plume) to maximum penetration—i.e., during the injection phase of the bubble plume (Table 1). The ability of dense plumes to obscure the image background was related to the existence of a significant population of large bubbles in the plume (Leifer and De Leeuw, 2006). The smallest diffuse bubble-plumes were segregated into the micro-plume class, which had fewer than 100 bubbles and were less than 10 cm wide and 10 cm deep. Many micro-plumes were significantly smaller. Also, several plume classes resulted from the interaction of two plumes formed in close proximity and time; however, these classes are not the subject of this study.

Plume life-phases were divided into formation, injection, rise, and senescence. Formation lasted 0.1 s or less and comprises the formation of bubbles from wave breaking including subsequent fragmentation. During injection, a downward jet from the wave-breaking advects bubbles to their injection depth. Once the plume reaches its maximum penetration depth, bubbles begin to rise, marking commencement of the rise phase. The senescence phase begins after the main plume mass reaches the surface and is comprised of the plume remnants. Thus, the plume lifetime, τ, is defined as comprising the injection and rise phases, but not the senescence phase. The plume lifetime, τ, was determined from the total bubble volume, $B_V(t)$, for the period when $B_V(t) > B_{VM}e^{-2}$, where B_{VM} is the maximum of B_V, which occurred at maximum penetration. The threshold at $B_{VM}e^{-2}$ provided a reasonable estimate of the transition between the rise and senescence phases.

Table 1
Bubble-plume classification criteria

Type	Symbol	Criteria
Broad	B	$w > 30$ cm
Narrow	N	$w < 30$ cm
Shallow	S	$z_P < 15$ cm
Deep	D	$z_P > 15$ cm
Dense	De	Background obscured by bubbles for entire injection phase
Diffuse	Di	Background not obscured by bubbles for entire injection phase
Micro		NSDi, $w < 10$ cm, $z_P < 10$ cm, $\Phi < 100$ (#)

w is the plume width, z_P is the maximum penetration depth and Φ is the total number of bubbles in the plume (population).

The bubble population size distribution, Φ (# μm^{-1}), was calculated for each plume class. Bubble distributions for the plumes are presented as populations rather than concentrations, φ (# μm^{-1} cm^{-3}), because Φ is approximately conserved during the injection phase, while φ decreases as the plume grows. Furthermore, for numerical model calculations of bubble-plume mediated processes, model initialization requires Φ. Φ is related to φ by $\Phi = P_V(t) * \varphi(t)$, where P_V is the plume volume and t is time. Typically, Φ (or φ) is represented by a power law of form,

$$\Phi(r,t) = r^{-S(t)} \tag{1}$$

where r is the equivalent spherical radius and S is the power law exponent and varies with t (Leifer and De Leeuw, 2006).

Class distributions were calculated by setting the time of maximum penetration to be the same for different plumes in each class and averaging $\Phi(r,t)$ for all plumes in each class. Plume-class characteristics were calculated from the class distribution. Injection size distributions, Φ_i, were calculated for maximum penetration. The lifetime-average size distributions, Φ_a, was the mean of $\Phi(r,t)$ for $t < \tau$.

The wave field was analyzed from time series of wave height measured by two high-resolution, capacitance wave-gauges described in Caulliez (2002) and Leifer et al. (2006). In this work, only fully developed breaking waves are considered, which were detected from the wave height signal using a geometric criterion based on a critical wave slope of 0.56 (Longuet-Higgins and Smith, 1983). The ratio of the time derivative of the wave-height signal to the mechanical-wave phase-speed determined by a cross-correlation method enabled us to estimate the instantaneous interface slope.

3. Results

3.1. Bubble plumes

Micro-plumes were the smallest and most common bubble-plume class, characterized by bubble-injection to only a few centimeters. The micro-plume class injection size distribution (Fig. 1) showed a characteristic injection size distribution, Φ_i, for the small bubbles of diffuse plumes; specifically, it decreased very shallowly ($\Phi_i \sim r^{-0.4}$) until a critical radius, R_C, of 1000 μm. For

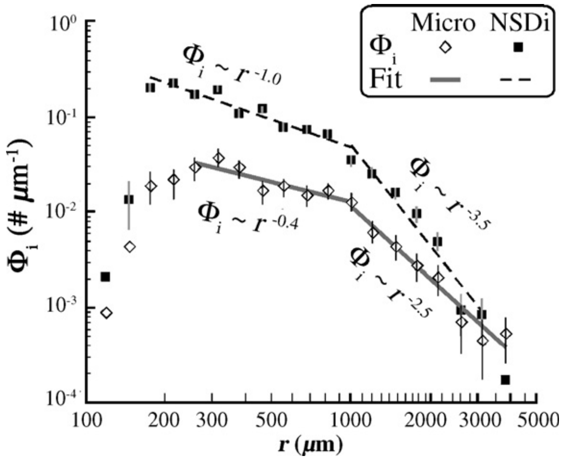

Fig. 1. Diffuse bubble classes' injection population size distribution, Φ_i, versus radius, r, and least-squares linear-regression analysis fit over range of fit. Data key on figure. Error bars $\pm\sigma$ (seven plumes analyzed).

$r>R_C$, Φ_i decreased more sharply ($\Phi_i \sim r^{-2.5}$). Even though $S<3$, total plume mass is not unbounded since the largest bubble observed for all plumes in the study was $r \sim 7000$ μm.

A plume class of larger (but also shallow) diffuse plumes, NSDi (Fig. 1), shows similarities to micro-plumes. Specifically, it exhibits a shallow small bubble population that decreases with $S=1.0$ until $R_C \sim 1000$ μm. For $r>R_C$, S increases sharply to $S=3.5$. For NSDi plumes, there is obvious size segregation with preferential injection of larger bubbles to shallower depths than smaller bubbles. Maximum penetration occurs 0.2 s after formation (i.e., the injection phase lasts ~0.2 s), while the rise phase lasts ~0.4 s.

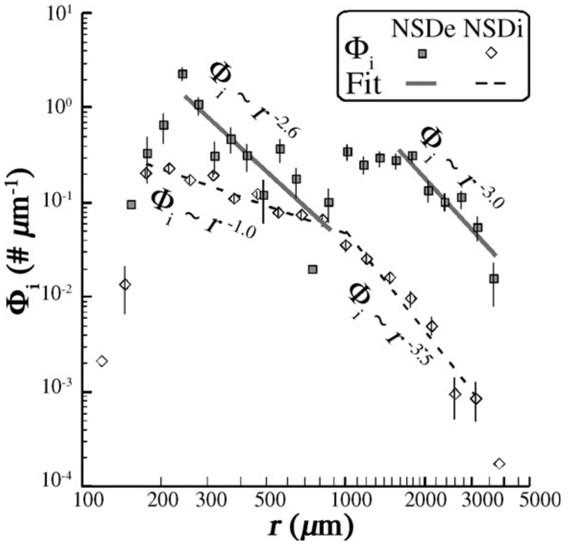

Fig. 2. NSDi and NSDe class injection population size distributions, Φ_i, as a function of radius, r, and least-squares linear-regression analysis fit over range of fit. Data key on figure. Error bars $\pm\sigma$.

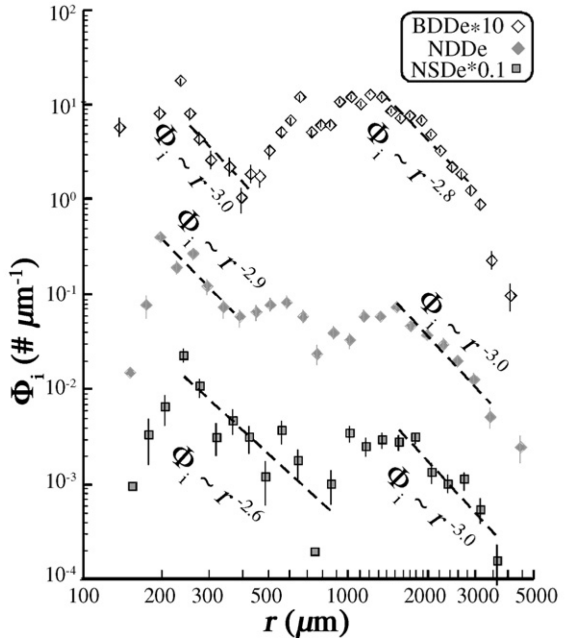

Fig. 3. Injection size distributions, Φ_i, as a function of radius, r, for NSDe, NDDe and BDDe classes and least-squares linear-regression analysis fit over range of fit. Note Φ_i for NSDe and BDDe are multiplied by factors of 0.1 and 10, respectively. Data key on figure. Error bars $\pm\sigma$.

A very distinctly different class of plumes was observed that are termed dense. Dense plumes exhibit a strong, large bubble peak centered at 1700 to 2000 μm. The most common and most characteristic dense plume class is the NSDe class (Fig. 2). For all dense plumes, small bubbles generally are injected significantly faster than larger bubbles. Thus, most small bubbles tend to be at the plume periphery, including deeper. The injection and rise phases both lasted ~0.25 s. Also, the transition between the injection and rise phases lasts longer for NSDe than for NSDi plumes.

The injection size distribution, $\Phi_i(r)$, shows significant differences between the NSDi and NSDe plume classes (Fig. 2). NSDi plumes are weakly r-dependent for $r<R_C$ and steeply decrease for $r>R_C$. In contrast, NSDe plumes are bi-modal with a first peak at 250 μm beyond which Φ_i decreases strongly with r and a second broad peak at 1700 μm that decreases even more sharply for larger r. Note how R_C for NSDi plumes is at the start of the "plateau" that extends to 1700 μm in the NSDe Φ_i. Also, because of the second large bubble peak, NSDe plumes have a significantly greater bubble volume, B_{VM},

Table 2
Bubble-plume class parameters for injection

Class	τ (s)	z_P (cm)	$\langle B_V \rangle$ (cm^3)	B_{VM} (cm^3)	P_{VM} (cm^3)	ε (%)	S_1 –	R_C (μm)	S_2
Micro	0.4	3.2	0.15	0.4	18	2.3	−0.4	1000	−2.5
NSDi	0.7	6	0.44	0.8	120	0.66	1.0	800	3.5
NSDe	0.9	9	1.9	3.8	460	0.81	2.6	1700	3.0
NDDe	1.2	23	2.8	4.8	2400	0.20	2.9	1600	3.0
BDDe	1.5	33	5.2	33	10,000	0.33	3.0	1500	2.8

τ is the plume lifetime, z_P is the maximum penetration depth, $\langle B_V \rangle$ is the average bubble volume during τ, B_{VM} and P_{VM} are the bubble and plume volumes at maximum penetration, respectively, ε is the void fraction, S is power law and R_C is the critical bubble radius where S changes. S_1, R_C, and S_2 from this study, other values from Leifer et al. (2006).

than NSDi plumes despite similar plume volume at the maximum penetration depth, P_{VM} (Table 2).

Both micro- and NSDi plumes show similar features, specifically, weakly size-dependent for $r<1000$ μm, and a more strongly decreasing, larger bubble regime. However, S for the larger NSDi plumes is greater both for bubbles larger and smaller than 1000 μm, the critical radius, R_C, than for micro-plumes. There are many similarities among the dense plume classes—NSDe, NDDe and BDDe (Fig. 3). There is a small bubble Φ_i that decreases approximately cubically from the lower size resolution limit. Note that NSDe plumes had so few small bubbles that statistics were poor. Also, in all classes, there is a small and poorly resolved peak at $r \sim 600$–700 μm, with the clearest evidence of this peak for NDDe plumes. Finally, there is a broad second peak at 1700 μm, with S approximately cubic. In the case of the NSDe and BDDe plumes, this peak spans $1000<r<1700$ μm.

Plume-class characteristics are summarized in Table 2. Void fraction, ε, is the ratio of B_{VM} to the plume volume, P_{VM}, at maximum penetration. Void fraction decreases as the plume expands during the injection phase and during the rise phase as bubbles are lost. At maximum penetration, the bubble population is still that of the plume formation or injection with the physical extent determined by the fluid motions (turbulent and bulk) induced by wave breaking, which inject the bubbles—i.e., the maximum potential energy occurs at maximum penetration. Thus, the void fraction at this moment is a proxy for the ratio of energy from wave breaking that is converted into the creation of surface area (bubble formation) to that which causes fluid motions including the injection jet. Interestingly, the smallest plumes had the highest void fraction and the largest plumes the lowest. Not surprisingly, diffuse and dense plumes of similar extent (e.g., NSDi and NSDe) showed much greater void fractions for dense plumes due to the large bubble contribution to dense plumes.

The formation rate of each plume class, P, was determined from analysis of overview camera video with respect to fetch. Determination of P in combination with Φ allowed estimation of the local (fetch-dependent) and global (fetch-integrated) injection population size distributions. These distributions and P were compared with wave characteristics. Interaction classes that resulted from the interaction of two plumes formed in close proximity were counted twice.

The formation rates for all diffuse, P_{Di}, and dense, P_{De}, plumes are strongly fetch-dependent (Fig. 4A). P_{De}

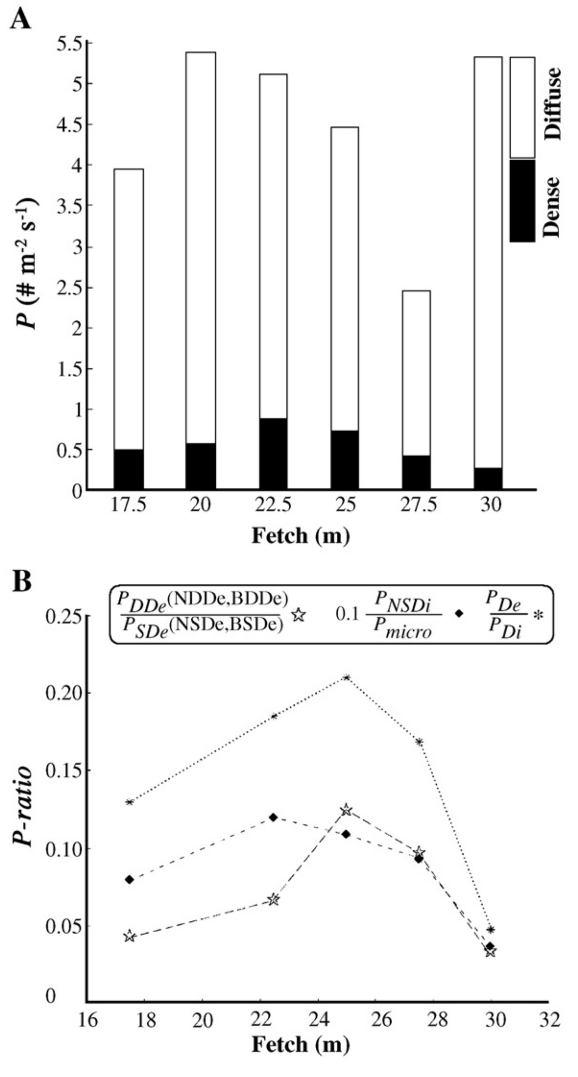

Fig. 4. (A) The formation rate, P, of dense and diffuse plumes with respect to fetch. Data key on figure. (B) Ratios of P for dense (P_{De}) to P for diffuse (P_{Di}) plumes, ratio of P for microplumes (P_{micro}) to P for narrow, shallow diffuse plume—NSDi (P_{NSDi}) and the ratio of deep to shallow plumes for deep and diffuse plumes for a single experiment. Observations were unavailable at 20-m fetch for this experiment. See text for further details. Data key on figure.

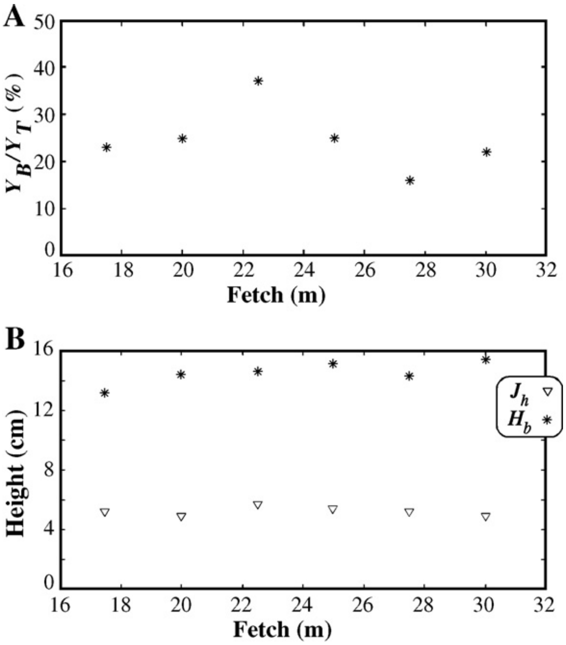

Fig. 5. (A) Percent of breaking waves Y_B/Y_T, where Y_B is the number of breaking waves and Y_T is total number of waves. (B) Fetch variation of the average trough-to-crest height, H_b, and average jump height, J_h, of the breaking waves versus fetch. These quantities were estimated for the wave signal samples recorded contemporaneously with the bubble-plume observations. Data key on figure.

increases to a maximum at 22.5 m, where, as discussed below, both visual observations and the evaluation of the percentage of breaking waves (Fig. 5A) indicate that wave breaking is at a maximum. Thereafter, P_{De} decreases with fetch. P_{Di} peaks earlier, at 20-m fetch, and then decreases until 27.5-m fetch, before dramatically increasing again. After its peak, P_{De} decreases more slowly than P_{Di}. As a result, the ratio P_{De}/P_{Di} peaks at 25-m fetch and then decreases afterwards. Among diffuse plumes, the peak in the ratio of micro- to NSDi plumes is at 22.5-m fetch, earlier than the peak in the ratio of P_{De} to P_{Di}. The ratio between the deep dense plume formation, P_{DDe} (i.e., P_{NDDe} and P_{BDDe}), and shallow dense plume formation, P_{SDe} ($P_{NSDe}+2*P_{BSDe}$), also shows a peak at 25-m fetch.

3.2. Wave characteristics

To describe wave-breaking conditions at the different fetches, the breaking rate was evaluated from the wave-height time series as the ratio between the number of fully developed breaking waves Y_B as detected by the geometrical criterion adopted above and the total number of waves observed Y_T. The ratio Y_B/Y_T is plotted in Fig. 5A for the same data as the bubble-plume observations shown in Fig. 4A. At these short fetches, the mechanical wave field is not in equilibrium with the wind and is the subject of crosswise large-scale wave modulation; thus, the wave-breaking rate is strongly fetch-dependent, with a clear maximum of ~35% at 23-m fetch. Immediately downstream, the breaking rate decreases sharply, indicating that the intense wave-field energy loss from wave breaking is not entirely compensated by direct input of wind energy. However, at 30-m fetch, the percentage of breaking waves increases again, thus suggesting the beginning of a new wave-breaking modulation cycle.

To be able to quantify to a certain extent the intensity of wave breaking in the study area, both the average trough-to-crest height, H_b, and the average jump height, J_h, of the breaking waves were estimated. J_h is the average height of the steep "turbulent" regions at the forward face of breaking-wave crests and is a good indicator of the wave energy dissipated by breaking (Caulliez, 2002). H_b varied weakly with fetch (Fig. 5B), first increasing until 20-m fetch, then remaining approximately constant between 20 m and 25 m, and then decreasing to a minimum at 28-m fetch before increasing again at 30-m fetch. J_h exhibits the same evolution with fetch as H_b, except that the maximum between 20-m and 25-m fetch is less pronounced and J_h continues decreasing at 30-m fetch. The evolution of these quantities clearly demonstrates that, even if the breaking rate exhibits a sharp peak at 23-m fetch, the breaking intensity is particularly high throughout the whole region located on both sides of this fetch. In contrast, both the breaking rate (Fig. 5A) and the breaking intensity as indicated by H_b (Fig 5B) are at a minimum at 28-m fetch.

The local injection population size distribution, ψ_i, at each fetch is shown in Fig. 6. ψ_i was calculated from

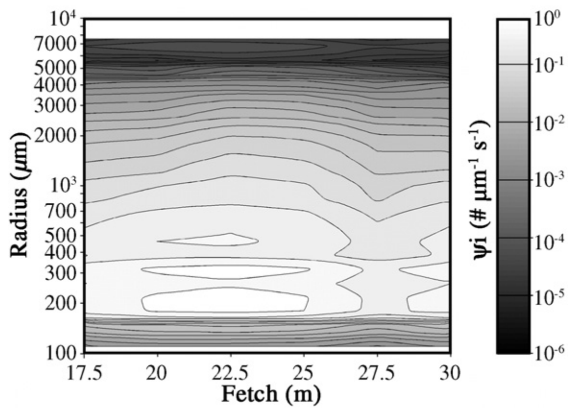

Fig. 6. Contour of the local, bubble injection population size distribution, ψ_i, with respect to radius and fetch.

the injection bubble-plume population size distributions, $\Phi_i(r)$, and the plume-class generation rate, P, using:

$$\psi_i(r) = \Sigma[P(X)\Phi_i(X,r)] \tag{2}$$

where X represents the different classes. The trend in ψ_i with fetch for larger bubbles (r>1000 μm) closely follows the trend in dense plumes, while for smaller bubbles (200<r<500 μm), the trend in ψ_i follows the trend in diffuse P. Specifically, dense plume P peaks at 22.5-m fetch and decreases thereafter, as does the population of large bubbles. The diffuse plume P peaks at 20-m fetch and again significantly at 30-m fetch. These trends are evident in the peak at 30-m fetch and in the broadness of the peak in ψ_i at 20–22 m for r<500 μm, which was skewed towards shorter fetches. Interestingly, for larger r, there is a plateau (1700<r<3500 μm) and a second peak (r~4500 μm) in ψ_i, both of which peak at 22.5 m, but extends from 20 to 27.5 m fetch, i.e., it is skewed towards greater fetch. The peak in ψ_i is at 22.5-m fetch due to the peak in P_{De} at 22.5-m fetch (Fig. 4A) and the shape of Φ_i for dense bubble plumes (Fig. 3). The skew relates to the ratio of P_{De}/P_{Di} (Fig. 4B) which peaks at 25-m fetch.

The global injection, total bubble population size distribution, $\Psi_i(r)$ (# μm^{-1} s^{-1}), was calculated by integrating ψ_i (Fig. 6) over the measured fetches. Roughly 47% of the injected bubble volume is contained in bubbles with r>1700 μm. The total injected bubble volume is 640 cm^3 of air per second into the area surveyed. The contribution from bubbles smaller than the non-invasive BMS resolution limit–r~200 μm–was negligible. Dense plumes contributed ~56% of the injected volume. The fetch-integrated global Ψ decreased as $\Psi_i \sim r^{-1.2}$ for r<1700 μm and $\Psi_i \sim r^{-3.9}$ for larger r (Leifer and De Leeuw, 2006).

4. Discussion

Two very distinct plume class types are observed, dense and diffuse, with very different Φ, in contrast to the great similarity in Φ between the different diffuse plume classes or between the different dense plume classes. Specifically, diffuse plumes have a broad, shallow Φ that decreases sharply for r>1000 μm. In contrast, dense plumes are multimodal with the small bubble Φ that decreases more steeply than for diffuse plumes and a second peak at r~1700 μm.

As a result, the large bubble population is significantly enhanced for dense plumes compared to diffuse plumes. It is these large bubbles that are responsible for obscuring the image background in the overview camera images. Dense plumes also exhibit greater B_V and P_{VM} than diffuse plumes indicating greater requisite formation energy. For example, although NSDi and NSDe plumes have similar dimensions, NSDe plumes persist longer, presumably due to greater turbulence.

Total plume formation, P_{Tot}, for all plumes trends with the diffuse plume P, P_{Di} (Fig. 4A). Both show a peak at 20 m, a monotonic decrease to a minimum at 27.5 m and a dramatic increase at 30-m fetch. Dense plume formation, P_{De} (Fig. 4A), breaking rate, Y_B/Y_T (Fig. 5A), and jump height, J_h, all peaked at 22.5-m fetch. The similarity in these trends indicates that wave development and bubble-plume formation are related. Note that the comparison between wave measurements and bubble-plume measurements involves a certain degree of uncertainty. While wave measurements are at a single point, bubble-plume observations are an average over the field of view; thus, comparison between the two is only to within ~50 cm. There also is a bias or offset due to the depth of the plume. Plumes required from 0.2 to 0.5 s for injection with deeper plumes requiring longer. During this time, the waves travel ~0.3 m to ~0.7 m; however, the combined uncertainty and bias in fetch are less than the distance between bubble-plume measurement fetches.

As noted, the wave field is not homogeneous with fetch due to large-scale wave modulation, although the wind stress is approximately constant over the modulation cycle. Thus, the evolution of the bubble-plume formation rate for dense and diffuse plumes can be studied with respect to wave development independently of variations in wind stress. As mentioned previously, one wave-modulation cycle occurs approximately between 14-m and 30-m fetches, with maximum wave development at 22.5-m fetch and minimum at 14-m and 28-m fetch. More precisely, at the beginning of the cycle, both the breaking rate and the breaking intensity as characterized by the breaking-wave height (or wave steepness because the mechanical-wave wavelength does not change with fetch) and jump height increase slowly. Then, a sharp maximum in wave-breaking rate is observed at 22.5-m fetch even though the most intense breaking occurs between 22.5-m and 25-m fetch. The minimum in wave breaking at 28-m fetch results from both a low breaking rate and smaller wave-breaking height.

The formation rate for the different bubble-plume classes varies strongly with fetch and in direct relation to the wave evolution and breaking. At the beginning of the wave modulation cycle, the formation of diffuse plumes, P_{Di}, increases sharply with a maximum at 20 m. Moreover, among these diffuse plumes, formation of the more energetic bubble plumes (NSDi) peaks at greater fetch than less energetic ones (micro). The maximum in dense plume formation, P_{De}, clearly is related to the maximum in the wave-breaking rate at 22.5-m fetch. Thus, the formation of the more energetic, dense bubble plumes appears to be linked to the wave-crest breakdown observed during intense wave breaking. Among these dense plumes, the most energetic ones, i.e., the deepest ones are observed in larger number at 25 m when the wave-breaking height is the greatest.

Between 25- and 27.5-m fetch, the wave field evolves due to wave dissipation from wave breaking superimposed on the effects of wave modulation and energy input from the wind. The increase in P_{Tot} at 30-m fetch is almost entirely due to diffuse plumes, about evenly split between NSDi and micro-plumes. This increase corresponds to a near disappearance of dense plume formation and an increase in both H_b and Y_B/Y_T. Thus, the generation of diffuse bubble plumes was related to the increase in wave breaking at 30 m. The trend for the dense plume P, P_{De}, is different with an increase to a peak at 22.5 m and then a monotonic decrease over the remaining fetches, including 30 m. This shows some similarities to the wave-breaking rate, Y_B/Y_T, which reaches a peak at 22.5-m fetch and then decreases until 28-m fetch.

Besides, not only is there a shift from dense to diffuse plumes beyond 25-m fetch, but there also are shifts within the class groups. There is a shift towards shallower, lower energy plumes in both diffuse and dense plumes, after peaks at 22.5 m and 25 m, respectively. For diffuse plumes, this manifests as a shift from NSDi to micro-plumes. Moreover, these shifts continue to 30-m fetch even though there is an increase in the breaking rate between 28- and 30-m fetch. These shifts likely are controlled most strongly by the large-scale modulation of the wave field.

To summarize these trends, with increasing bubble-plume energy, the peak in P occurs at greater fetch. Thus, P_{Di} peaks at 20-m fetch, P_{De} at 22.5-m fetch and the largest dense plumes (BDDe and NDDe) at 25-m fetch. The same held true within these two categories of classes. NSDi plumes relative to micro-plumes peak at 22.5-m fetch, not 20.0 m, and NSDe plumes peaks at 22.5 m, not 25 m. Similarly, the recovery at 30 m in P_{Tot} is solely due to micro-plumes, all other plume classes continue decreasing.

The differences between dense and diffuse plumes suggest two different formation mechanisms. If we hypothesize that there are two different wave-breaking modes that correspond to these different bubble-plume formation mechanisms, then the diffuse plume formation mechanism develops until 22.5-m fetch, while the dense-plume formation mechanism develops until 25-m fetch. In addition, as wave breaking becomes more intense, the production rate of the most energetic plumes increase and the intensity (or size) of both diffuse and dense plumes—i.e., the wave-breaking energy, increases in both modes. This likely relates to the production of larger plumes within these groups of classes. Also, both waves and wave breaking evolve due to wave-field modulation. This explains the sharp decrease in P at 27.5-m fetch and the shift in plume generation within each plume group towards less energetic plumes and between plume groups towards diffuse plumes. Although the mechanisms for the formation of these plumes are unknown, there clearly is a relationship between the wave-breaking parameters that describe full wave-breaking and dense plume formation.

The shifts in P with fetch are at the origin of the changes in the global bubble population. Although P_{Di} reaches a peak at 20-m fetch, because NSDi plumes contain far more bubbles, the small bubble population peaks at 22.5-m fetch. There still is significant production of the smallest bubbles at 25-m fetch; however, the small bubble distribution steepens due to the importance of small bubble production from dense plumes. At 30-m fetch, where micro-plumes are overwhelmingly dominant, the small bubble distribution is only weakly dependent on bubble size. Meanwhile, the larger bubble population (unsurprisingly) tracks P_{De}. The production of 1700-μm radius bubbles (i.e., the radius of the larger, dense plume peak) was approximately constant between 22.5- and 25-m fetch. This is because, although the larger NDDe and BDDe plumes were much less common, they contributed far more bubbles than NSDe plumes. Interestingly, the very largest bubbles, $r > 5000$ μm, were produced most strongly at 22.5-m fetch, not 25-m fetch. One possible explanation may be that the most intense plumes tended to fragment these largest bubbles.

4.1. Application to the ocean

Results of this study were for fresh water. Thus, consideration of these results with respect to the ocean requires understanding of the significant effect of salinity on bubble formation. In whitecap simulation tank (WST) experiments, Haines and Johnson (1995) showed a similar S for large bubbles in fresh- and saltwater ($S = 2.7$, $S = 2.6$, respectively, for r greater than a critic radius, R_C); however, R_C was at much larger r for fresh ($R_C \sim 2800$ μm) than salt ($R_C \sim 630$ μm) water. As a result, small ($300 < r < 600$ μm) bubble concentrations were much larger in saltwater than fresh water, while large ($r > 2000$ μm) bubble concentrations were slightly greater in fresh water. Using laser bubble measurements in a WST, Asher et al. (1997) observed a similar slope in

φ for salt and fresh water (S unreported), with higher concentrations for small salt–water bubbles. "Small" was defied as bubbles with $r<200$ and $r<400$ µm for fresh- and saltwater, respectively. The freshwater φ had a peak or a plateau at 500 µm, and as a result the freshwater concentration of bubbles larger than $r\sim200$ µm was greater than for saltwater. Part of the discrepancy between these two data sets may have resulted from wall effects in Haines and Johnson (1995) WST. For mechanically generated, breaking-wave bubble plumes, Loewen et al. (1996) found little difference for larger bubbles ($1000<r<4000$ µm) between fresh- and saltwater for focused waves. For wind-generated breaking waves, Cartmill and Su (1993) showed that, for $50<r<1000$ µm, far more small bubbles (an order of magnitude) were produced in saltwater than freshwater. In summary, wave-breaking and WST results are in general agreement that the fresh- and saltwater size distribution for larger bubbles is similar. There is also agreement that far more small bubbles are produced in saltwater. Because large bubbles contain most of the plume mass, total gas injection appears to be largely independent of salinity (Wu, 2000). Thus, we argue that our findings with respect to bubbles larger than about 700-µm radius should be roughly applicable to ocean waves given similar wave-breaking conditions.

In this study it was found that for diffuse-plumes, the injection Φ was very weakly dependent on r, with S varying between 0.4 (micro) and 1.3 (NSDi) for small bubbles ($r<1000$ µm). This shallow S during injection agrees with other observations that Φ is significantly shallower closer to the formation region or time, than the background population, which is temporally and spatially averaged—e.g., Baldy and Bourguel (1987). The plume investigated by Haines and Johnson (1995) exhibited aspects of diffuse plumes (i.e., many small bubbles and a critical radius) and aspects of dense bubble plumes (a peripheral region with small bubbles and a large radius peak in the size distribution). However, Haines and Johnson (1995) studied plumes in a WST—i.e., tipping bucket formation mechanism, thus, classification as dense or diffuse may be inappropriate. Deane and Stokes (2002) reported $S=1.8$ for an individual ocean bubble plume observed at an undetermined time after formation. The small bubble population was much higher than those observed for dense bubble plumes in Luminy and may have been due to salinity or other factors.

5. Conclusion

This study aimed to describe the characteristics of the plume bubbles generated by wind-stress wave breaking and relate the types of plumes formed and the formation rates to waves and wave breaking. The study showed the existence of two distinct classes of bubble plumes respectively termed dense and diffuse, which are characterized by the presence or absence of large bubbles. This finding is based on the analysis of the bubble size distributions of bubble plumes. Bubble plumes were segregated based on their maximum penetration depth, their lateral extent and their ability to obscure optically the image background. This obscuration was due to the presence of large bubbles (dense plumes). The bubble size distributions of dense plumes exhibit a significant population of very large bubbles (radius greater than 1 mm). In contrast, diffuse plumes were largely lacking in these very large bubbles. Given that many bubble processes are strongly radius-dependent, this implies that the impact of the two plume classes on bubble-mediated processes should be highly distinct. Furthermore, the occurrence of both groups of bubble-plume classes is highly dependent on wave-breaking development with dense plumes forming preferentially under conditions of intense full wave breaking and diffuse plumes forming preferentially at the earlier stages of wave-breaking events. These observations suggest these two bubble-plume classes are related to two different plume formation processes associated with the wave-breaking process.

Given that the formation of the different plume classes was related closely to wave breaking and wave development, we hypothesize that the two different groups of bubble-plume classes–dense and diffuse–may occur at sea, too. Oceanic measurements of the background population show strong variation with wind stress and fetch among other factors. Thus, these results suggest that some of the variability in the bubble field data may result from variations in the different modes of bubble-plume formation, which are related to wave-breaking development and the sea state. Clearly, to understand the underlying processes that produce the background bubble population, further research into bubble plumes in the field and laboratory are required.

Acknowledgement

Most of the work reported here was carried out as part of the LUMINY project which was supported by the European Commission EC DG XII, contract ENV4-CT95-0080, and for the part of TNO-FEL, with additional support from the Netherlands Ministry of Defense, assignment A95KM786. Part of the work of Dr. Leifer was carried out while employed by the National University of Ireland in Galway and when he was a visiting-scientist at TNO-FEL. The authors would like to thank IRPHE-IOA for the extensive laboratory support provided during LUMINY experiments.

References

Asher, W.E., Karle, L.M., Higgins, B.J., 1997. On the difference between bubble-mediated air-water transfer in freshwater and seawater. J. Mar. Res. 55, 1–34.

Baldy, S., Bourguel, M., 1987. Bubbles between the wave trough and wave crest levels. J. Geophys. Res. 92C3, 2919–2929.

Cartmill, J.W., Su, M.Y., 1993. Bubble size distributions under saltwater and freshwater breaking waves. Dyn. Atmos. Ocean. 20, 25–31.

Caulliez, G., 2002. Statistics of geometric properties of breaking wind waves observed in laboratory. In: Donelan, M., Drennan, W., Salzman, E.S., Wanninkhof, R. (Eds.), Gas Transfer and Water Surfaces, vol. 127. AGU, pp. 31–37.

Clift, R., Grace, J.R., Weber, M.E., 1978. Bubbles Drops and Particles. Academic Press, New York/New York, p. 380.

De Leeuw, G., 1990. Spray droplet source function: from laboratory to open ocean. In: Mestayer, P.G., Monahan, E.C., Beetham, P.A. (Eds.), Modeling the Fate and Influence of Marine Spray. Proc. of a Workshop held on 6–8 June 1990, Luminy, Marseille, France, pp. 17–28.

De Leeuw, G., Cohen, L.H., 2002. Bubble size distributions on the North Atlantic and North Sea. In: Donelan, M.A., Drennan, W.M., Salzman, E.S., Wanninkhof, R. (Eds.), Gas Transfer and Water Surfaces. Geophysical Monograph, vol. 127. American Geophysical Union, Washington D.C., pp. 271–277.

De Leeuw, G., Kunz, G.J., Caulliez, G., Jaouen, L., Badulin, S., Woolf, D.K., Bowyer, P., Leifer, I.S., Nightingale, P., Liddicoat, M., Rhee, T.S., Andreae, M.O., Larsen, S.E., Hansen, F. Aa., Lund, S., 1999. Breaking waves and air–sea gas transfer (LUMINY), Contract ENV4-CT95-0080. In: de Leeuw, G. (Ed.), Final Report: 1 February 1996–31 January 1999. TNO Physics and Electronics Laboratory, Report FEL-99-C122.

De Leeuw, G., Kunz, G.J., Caulliez, G., Woolf, D.K., Bowyer, P., Leifer, I., Nightingale, P., Liddicoat, M., Rhee, T.S., Andreae, M.O., Larsen, S.E., Hansen, F. Aa., Lund, S., 2002. LUMINY—an overview. In: Donelan, M., Drennan, W., Salzman, E.S., Wanninkhof, R. (Eds.), Gas Transfer and Water Surfaces, vol. 127. AGU, pp. 291–294.

Deane, G.B., Stokes, M.D., 2002. Scale dependence of bubble creation mechanisms in breaking waves. Nature 418, 839–843.

Haines, M.A., Johnson, B.D., 1995. Injected bubble populations in seawater and fresh water measured by a photographic method. J. Geophys. Res. 100C4, 7057–7068.

Kitaigorodskii, S.A., 1984. Wind-wave effects on gas transfer. In: Brutsaert, W., Jirka, G.H. (Eds.), Gas Transfer at Water Surfaces. Reidel Publishing Company, Hingham, Massachusetts, pp. 141–170.

Leifer, I., De Leeuw, G., 2006. Bubbles generated from wind-steepened breaking waves: Part 1. Bubble plume bubbles. J. Geophys. Res. 111, C06020. doi:10.1029/2004JC002673.

Leifer, I., De Leeuw, G., Cohen, L.H., 2003. Optical measurement of bubbles: system design and application. J. Atmos. Ocean. Technol. 20 (9), 1317–1332.

Leifer, I., Caulliez, G., De Leeuw, G., 2006. Bubbles generated from wind-steepened breaking waves: Part 2. Bubble plumes, bubbles, and wave characteristics. J. Geophys. Res. 111, C06021. doi:10.1029/2004JC002676.

Liss, P.S., Watson, A.J., Bock, E.J., Jähne, B., Asher, W.E., Frew, N.M., Hasse, L., Korenowski, G.M., Merlivat, L., Phillips, L.F., Schluessel, P., Wolf, D.K., 1997. Physical processes in the microlayer and the air–sea exchange of trace gases. In: Liss, P.S., Duce, R.A. (Eds.), The Sea Surface and Global Change. Cambridge University Press, Cambridge, UK, pp. 1–33.

Loewen, M.R., O'Dor, M.A., Skafel, M.G., 1996. Bubbles entrained by mechanically generated breaking waves. J. Geophys. Res. 101, 20759–20769.

Longuet-Higgins, M.S., Smith, N.D., 1983. Measurement of breaking by a surface jump meter. J. Geophys. Res. 88, 9823–9831.

Medwin, H., Breitz, N.D., 1989. Ambient and transient bubble spectral densities in quiescent seas and under spilling breakers. J. Geophys. Res. 94C, 12,751–12,759.

Monahan, E.C., Dam, H.G., 2001. Bubbles: an estimate of their role in the global oceanic flux of carbon. J. Geophys. Res. 105 C5, 9377–9383.

NIH Software, developed at the U.S. National Institutes of Health and available on the Internet at http://rsb.info.nih.gov/nih-image/, 2001.

O'Dowd, C.D., Facchini, M.-C., Cavilli, F., Ceburnis, D., Mircea, M., Decesari, S., Fuzzi, S., Yoon, Y.J., Putaud, J.-P., 2004. Biologically driven organic contribution to marine aerosol. Nature 431, 676–680.

Woolf, D.K., 1997. Bubbles and their role in gas exchange. In: Liss, P.S., Duce, R.A. (Eds.), The Sea Surface and Global Change. Cambridge University Press, Cambridge, UK, pp. 174–205.

Wu, J., 2000. Bubbles produced by breaking waves in fresh and salt waters. J. Phys. Oceanogr. 30, 1809–1813.